

# A Computational Analysis of the Influence of Anastomosis Angle on Stenosis-Prone Locations during Radio-Cephalic Arteriovenous Fistula Maturation

Yang Yang<sup>1</sup> , Pascale Kulisa<sup>2</sup>, Benyebka Bou-Saïd<sup>1,3</sup>, Mahmoud El Hajem<sup>4</sup>, Serge Simoens<sup>2</sup> , Nellie Della Schiava<sup>5</sup> 

<sup>1</sup>CNRS, INSA de Lyon, LaMCoS, University of Lyon, Villeurbanne, France; <sup>2</sup>INSA Lyon, CNRS, Ecole Centrale de Lyon, Univ Claude Bernard Lyon 1, LMFA, University of Lyon, Villeurbanne, France; <sup>3</sup>State Key Laboratory of Solidification Processing, Center of Advanced Lubrication and Seal Materials, Northwestern Polytechnical University, Xi'an, China; <sup>4</sup>CNRS, Ecole Centrale de Lyon, INSA Lyon, Univ Claude Bernard Lyon 1, LMFA, University of Lyon, Ecully, France; <sup>5</sup>Department of Vascular Surgery, Hospices Civils de Lyon, Lyon, France

**Correspondence to:** Yang Yang, 1001yyang@gmail.com

**Keywords:** Radio-Cephalic Arteriovenous Fistula (RCAVF), Anastomosis Angle, Maturation, Wall Shear Stress Distribution, Stenosis-Prone Locations

**Received:** June 1, 2023

**Accepted:** June 27, 2023

**Published:** June 30, 2023

Copyright © 2023 by author(s) and Scientific Research Publishing Inc.

This work is licensed under the Creative Commons Attribution International License (CC BY 4.0).

<http://creativecommons.org/licenses/by/4.0/>



Open Access

## ABSTRACT

In dialysis treatment, the radio-cephalic arteriovenous fistula (RCAVF) is a commonly used fistula, yet its low maturation rate remains a challenge. To enhance surgical outcomes, the relationship between stenosis-prone locations and RCAVF anastomosis angle is studied during maturation by developing two sets of RCAVF models for early (non-mature) and mature RCAVFs at five anastomosis angles. The impact of hemodynamics and wall shear stress (WSS) is examined to determine optimal anastomotic angles. Results indicate that acute angles produce more physiological WSS distributions and fewer disturbed regions, with early stenosis-prone regions located near the anastomosis that shift to the bending venous segment during remodeling. A pilot study comparing clinical and numerical results is conducted for validation.

## 1. INTRODUCTION

Untreated chronic kidney disease can result in end-stage renal disease (ESRD) [1]. Dialysis treatment through arteriovenous fistulas (AVFs) is the most common method of sustaining ESRD patients' lives [2]. In France, there are over 10,000 AVF creations annually, surpassing the number of aortic surgeries. The incidence of ESRD continues to increase, with approximately 8000 deaths and 11,000 new cases per year (Data provided by Hospices Civils de Lyon). The radio-cephalic arteriovenous fistula (RCAVF) is frequently recommended as the preferred AVF [3], however, its susceptibility to early failure [3] highlights

the importance of careful vessel selection and anastomosis design in RCAVF.

The maturation of fistulas and the development of stenosis are complex biological and mechanical phenomena. The vessels must rapidly undergo remodeling to enhance blood flow [4]. During maturation, disturbed flow near the anastomosis is formed as a result of vascular remodeling and increased blood flow [5]. The low and oscillating wall shear stress (WSS) generated by the disturbed flow has a negative impact on the vascular wall, hastening stenosis progression [6]. Computational modeling is an effective method for providing surgeons with visual and analytical insights into the fistula's hemodynamics.

In the previous work, we discovered that the anastomosis angle ( $\theta$ ) significantly affected energy loss in RCAVF [7] (the friction and the presence of disturbed fluid were the main causes of energy loss). This research focuses on the effect of  $\theta$  during the maturation on disturbed flow and aims to identify stenosis-prone locations (SPL) in both pre- and post-operative stages. The findings are compared with previous clinical observations [8]. A pilot study of six cases comparing clinical and numerical results is also conducted for validation.

## 2. MATERIALS AND METHODS

Two sets of RCAVF models with varying  $\theta$  are established by Catia V5-6R2012. The RCAVF can be separated into four segments: proximal radial artery (PRA), distal radial artery (DRA), bending cephalic vein (BCV), and normal cephalic vein (NCV) (Figure 1(a)). Non-mature models present the RCAVFs in the early mature stage that has just been anastomosed. The radial artery (RA) diameter ( $D_{ra}$ ), cephalic vein (CV) diameter ( $D_{cv}$ ),  $h$ , and  $D_a$  (Figure 1(a)) were obtained via duplex ultrasound (DUS) from an actual patient whose anastomosis was established on March 7, 2019 (Data provided by Hospices Civils de Lyon). The  $\theta$  varied among  $30^\circ$ ,  $45^\circ$ ,  $60^\circ$ ,  $75^\circ$ , and  $90^\circ$ . Mature models were generated based on DUS measurements taken several weeks (April 26, 2019) after the fistula creation and depict the RCAVF models in a mature stage ready for dialysis treatment. The  $D_{ra}$  and  $D_{cv}$  were observed to have dilated to 3 mm and 6.1 mm, respectively, while  $D_a$  and  $h$  remained unchanged, and  $\theta$  varied in the same manner as in the non-mature models.

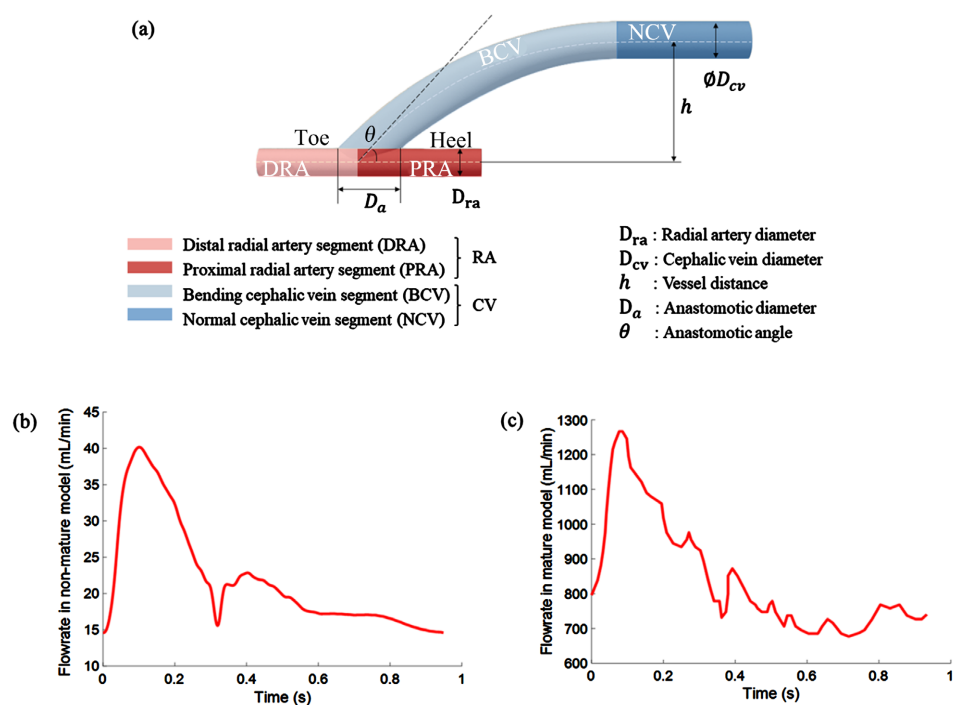


**Figure 1.** (a) The radio-cephalic arteriovenous fistula (RCAVF) model. (b) The flowrate waveform at the PRA inlet in non-mature models. (c) The flowrate waveform at the PRA inlet in mature models.

The flow of blood is modeled as a three-dimensional, unsteady, incompressible Newtonian fluid. The density and viscosity are defined by 1060 kg/m<sup>3</sup> [9] and 0.0035 Pa's [10], respectively. After a convergence study, we use STAR-CCM+ 2020.2.1 (15.04.010) to discretize the models into a polyhedron mesh with a 0.1 mm mesh size. The Navier-Stokes equations were solved by an Euler implicit time scheme. The simulation is conducted with solver pisoFoam [11] in Foamextend 4.0 with a time step of 1e-4s, and considered converged after three cardiac cycles.

A fully developed Poiseuille flow profile is created at the inlets by Matlab R2021b. A constant pressure of 8.7 mmHg [12] is applied to the vein outlet. In non-mature models, the DRA inlet is set to a constant flow rate ( $Q_{DRA}$ ) of 5 ml/min, calculated by multiplying the average blood velocity at the wrist [13] by the smallest RA cross-section [14]. A pulse flow with a mean blood flow ( $Q_{PRA}$ ) of 22 ml/min [15] is set at the PRA inlet (Figure 1(b)). In mature models, the flow rates are measured by DUS. The  $Q_{DRA}$  was a 60 ml/min constant flow. The  $Q_{PRA}$  equaled 871 ml/min (Figure 1(c)).

We performed hemodynamic and WSS analyses for all the models. We observed velocity fields, streamlines, and localized normalized helicity (LNH) in hemodynamic analysis. With the regrouping of vessel structures, helical flow occurs in the RCAVF. The presence of helical flow can stabilize the flow fields and reduce the disturbed shear [16-18], which minimizes the low and oscillating WSSs and reduces the stenosis risk [19]. A threshold of  $\pm 0.9$  for LNH is used to detect the flow helicity in the fistula [20]. We used three WSS biomarkers: time-averaged WSS (TAWSS) [4], oscillatory shear index (OSI) [5, 21] and relative residence time (RRT) [22, 23] to find the low WSS, oscillating WSS, and stenosis-prone regions. Their definitions are described by the following equations:

$$TAWSS = \frac{1}{T} \int_0^T |\tau_w| dt \quad (1)$$

$$OSI = \frac{1}{2} \left( 1 - \frac{\left| \int_0^T \tau_w dt \right|}{\int_0^T |\tau_w| dt} \right) \quad (2)$$

$$RRT \sim \left[ (1 - 2 \cdot OSI) \cdot TAWSS \right]^{-1} \quad (3)$$

where  $\tau_w$  is WSS vectors. A cardiac cycle is represented by  $T$ . The RRT is normalized by a reference value derived from the time-averaged fully developed blood volume flow in the straight CV segment in the lower forearm. An RRT value is greater than one denotes either regions with low WSSs or regions with both low and oscillating WSSs [23].

### 3. RESULTS

#### 3.1. Non-Mature Models

The hemodynamic behaviors are shown in Figure 2. The results indicated the presence of low-velocity zones (LVZs) surrounding the anastomosis (Figure 2(a)). A recirculating eddy is observed at the heel of the anastomosis, with a larger range in systole compared to end-diastole (Figure 2(b)). The 90° model shows a larger reflux region compared to the 30° model. The helicity contents for different  $\theta$  followed a similar trend to the reflux regions for different  $\theta$  (Figure 2(c)). The highest elevated LNH region is found in the 30° models.

The results of the three WSS biomarkers for the 30° and 90° non-mature models are presented in Figure 3. The magnitude of shear in the arterial system ranges from 1 to 7 Pa, and in the vein, it varies from 0.1 to 0.6 Pa [24]. The low TAWSS region, indicated by navy blue in Figure 3(a), is defined as the region with TAWSS values less than 0.1 Pa. The WSS in this region is lower than the normal range for the venous system, due to the resistances created by the DRA inlet, the anastomosis, and the venous bending section, which impede the blood flow entering from the PRA inlet. The low TAWSS regions are observed around the anastomosis (Figure 3(a)). The minimum TAWSS values near the anastomosis's toe (Toe\_min), heel (Heel\_min), and floor (Floor\_min) were calculated (Table 1). Additionally, the total surface areas of

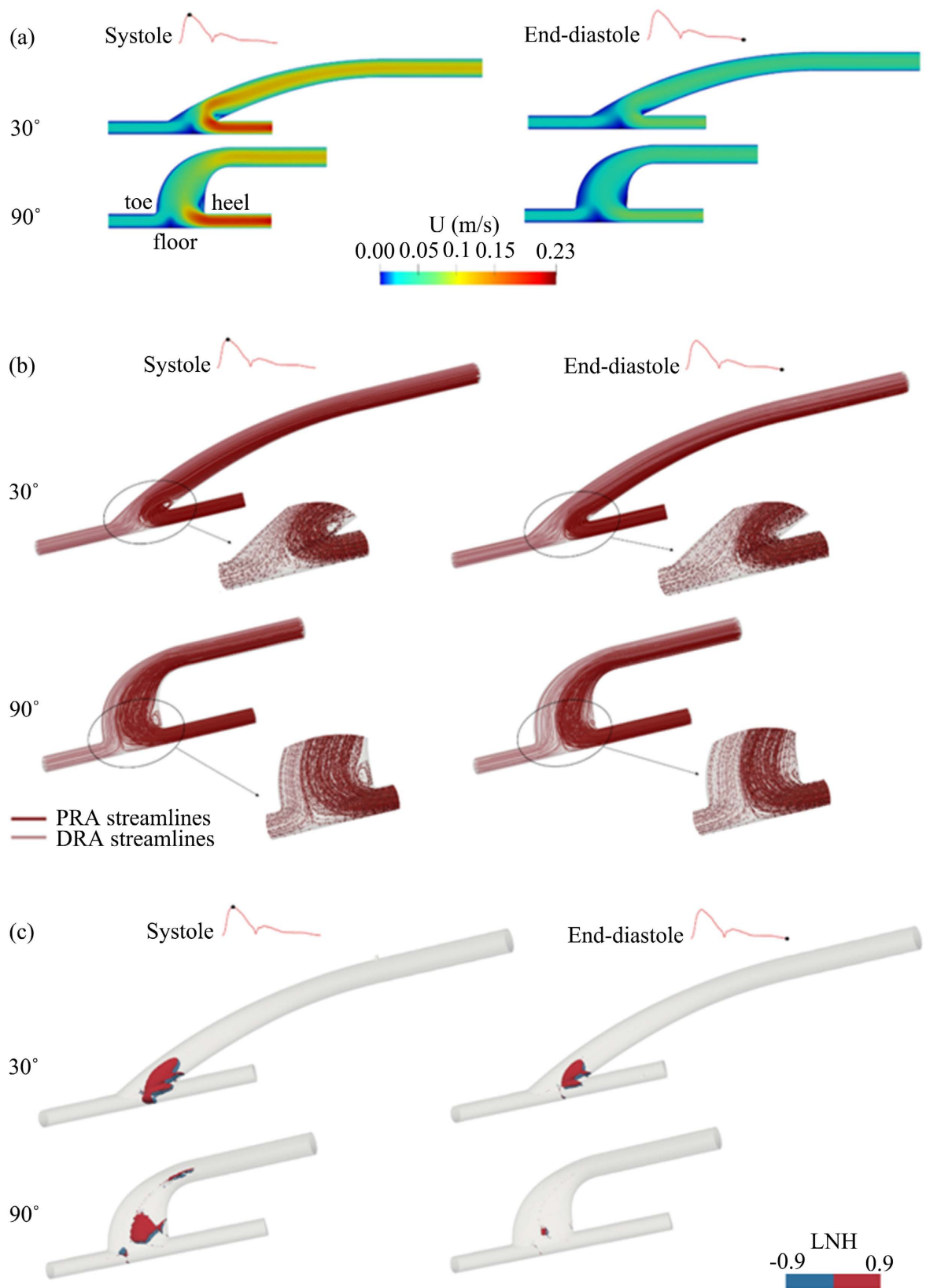


**Figure 2.** Comparisons of hemodynamics in non-mature models. (a) Velocity fields; (b) Streamlines; (c) LNH distributions.

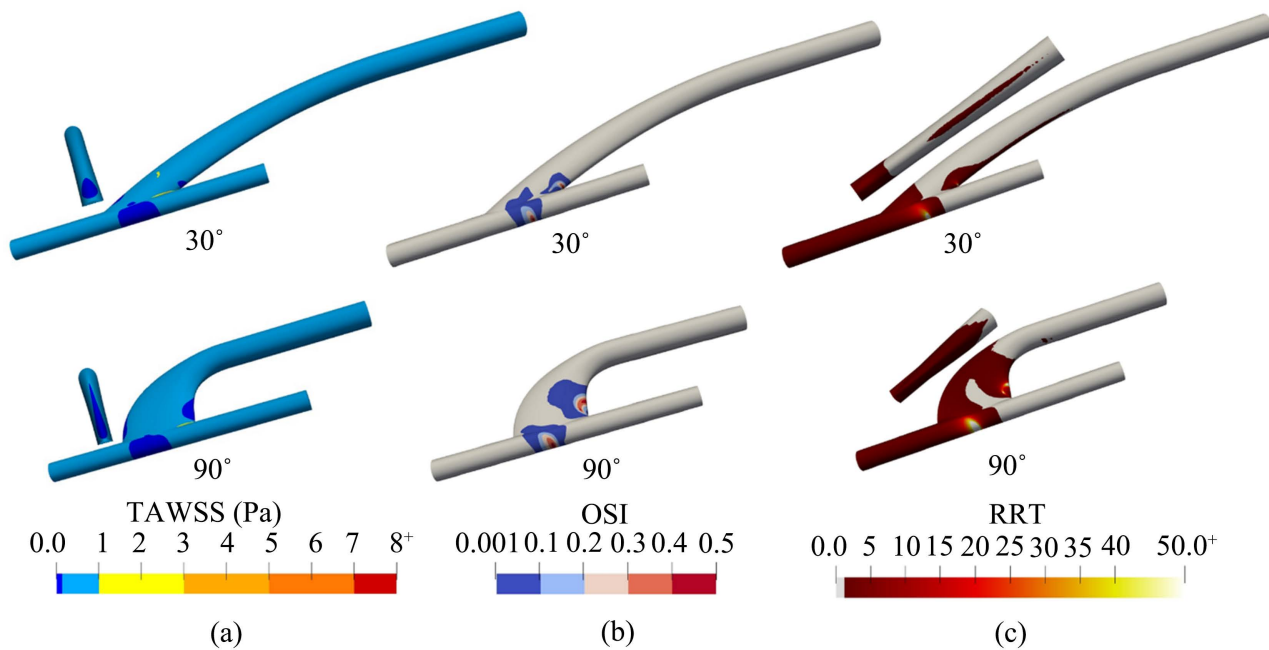


**Figure 3.** Comparisons of WSS biomarkers in non-mature models. (a) TAWSS distributions; (b) OSI distributions; (c) RRT distributions.

**Table 1.** Comparison of three WSS biomarkers in non-mature models.

θ (°)	TAWSS				OSI	RRT		
	CV		RA					
	Toe_min <sup>a</sup> (Pa)	Heel_min <sup>b</sup> (Pa)	CV_area <sup>c</sup> (mm <sup>2</sup> )	Floor_min <sup>d</sup> (Pa)				
30	0.55	0.64	11.00	0.23	25.17	54.49	237.43	186.11
45	0.37	0.46	19.36	0.20	25.85	89.14	299.65	570.14
60	0.32	0.39	23.33	0.20	25.37	120.36	311.38	708.18
75	0.30	0.36	23.61	0.19	25.32	123.69	343.64	1559.98
90	0.32	0.41	21.61	0.20	25.56	118.37	330.15	1511.11

a. The minimal TAWSS value in low TAWSS region near the toe of anastomose. b. The minimal TAWSS value in low TAWSS region near the heel of anastomose. c. The total area of low TAWSS region in CV. d. The minimal TAWSS value in low TAWSS region near the floor of anastomose. e. The total area of low TAWSS region in RA. f. The total area of OSI higher than 0.001. g. The total area of RRT larger than 1. h. The maximal RRT value.

the low TAWSS regions in the vein (CV\_area) and artery (Floor\_area) were determined. The 30° model has the largest Toe\_min value, while the trends of Heel\_min are in contrast to CV\_area. The CV\_area increases rapidly from 30° to 60°, reaching a peak at 75°, before experiencing a slight decline at 90°. The change of Floor\_min is consistent with the Floor\_area, which can be considered constant.

In **Figure 3(b)**, regions with low OSI values, defined as less than 0.001 [25], are depicted in gray. The color intensity in the remaining areas represents the magnitude of OSI, with warmer colors indicating higher OSI values. The high OSI regions indicate the presence of oscillating WSS near the heel and floor of the anastomosis, where disturbed flows exist. The total surface area with OSI values greater than 0.001 (OSI\_area) has been calculated (**Table 1**), and it shows a trend similar to that of the low TAWSS regions in CV. These results suggest that the impact of oscillating WSS is more pronounced on the RCAVF with larger values of  $\theta$ .

**Figure 3(c)** displays the RRT of the models at 30° and 90°. The RRT values lower than 1 are shown in gray. The RRT values larger than 1 indicates areas may have the stenosis risk [23]. The larger the RRT value, the brighter the color. As  $\theta$  increases, the high RRT values (RRT > 1) develop from the anastomosis' toe to the NCV segment along the BCV segment. The total area of an RRT value larger than 1 (RRT\_area shown in **Table 1**) is continuously increasing from 30° to 75°, with the maximal RRT value (RRT\_max) being found in the 75° model. However, in the 90° model, both RRT\_area and RRT\_max slightly decrease. Beyond 60°, the high RRT values almost completely cover the BCV segment at the toe side.

In conclusion, the acute  $\theta$  with the higher helicity results in a more stable flow and a better WSS distribution.

### 3.2. Mature Models

In the mature models (as illustrated in **Figure 4(a)**), it has been observed that there has been a significant increase in the extent of disturbed regions. An analysis of the BCV segment reveals that approximately half of the segment's area is occupied by the recirculating region, as depicted in **Figure 4(b)**. The majority of the streamlines in the recirculating region are observed to originate from the DRA inlet. Additionally, a second, smaller reflux region is observed within the BCV segment, which is generated in the largest recirculating region near the heel of the anastomosis, and this occurs when  $\theta$  is greater than 60°. The streamlines at systole in the recirculating region were separately analyzed and presented in the third row of **Figure 4(b)**. Ten streamlines were randomly selected from the largest recirculating region, which are depicted as blue lines. Conversely, four streamlines were extracted from the smallest recirculating region generated in the large- $\theta$  models ( $\theta > 45^\circ$ ), and are represented by red lines. As  $\theta$  increases from 30° to 60°, a decrease in the number of streamlines entering from the PRA inlet and flowing into the recirculating region is observed, followed by an increase when  $\theta$  is greater than 60°. This small recirculating region is primarily attributed to the DRA inlet. The LNH distributions, as illustrated in **Figure 4(c)**, demonstrate that the largest elevated LNH region continues to be present in the 30° RCAVF models.

The vein is successfully rebuilt and resembles the artery in the mature RCAVF. As a result, a comparison of the WSS values was made with the normal arterial WSS range, which is between 1 and 7 Pa [24]. In **Figure 5(a)**, the blue regions represent areas that exhibit low TAWSS values (<1 Pa), and these are observed around the anastomosis. The minimum TAWSS values (values lower than 1 Pa) and the total area of low TAWSS in the CV and RA are presented in **Table 2**. It was noted that the Toe\_min value decreases from 30° to 45°, then increases after 45°, and surpasses 1 Pa in the 90° model. The Heel\_min value is only present in large- $\theta$  models. Therefore, there is a rapid increase in the CV\_area in the 60° models. The Floor\_min and Floor\_area values in the RA do not show significant variations with  $\theta$ .

As the mature models mature, the dimensions of the disturbed fluid increase, leading to a corresponding increase in the oscillating WSS. The high OSI regions are predominantly located along the BCV segment at the boundaries of the recirculating regions, as illustrated in **Figure 5(b)**. As  $\theta$  continues to increase, as seen in the 60° model, the emergence of a new recirculating region results in the development of an oscillating region near the heel of the anastomosis.

In comparison to the non-mature case, the RRT values are significantly reduced in the mature models, as a result of vessel remodeling, as indicated in **Figure 5(c)**. The maximum RRT values are observed near the heel of the anastomosis in large- $\theta$  models, at the toe of the anastomosis in the 45° model, and at the entrance of the straight vein in the 30° model. However, the average RRT (RRT\_ave) values in the colored area of the small- $\theta$  ( $\theta \leq 45^\circ$ ) models are lower than those of the large- $\theta$  models, as presented in **Table 2**.

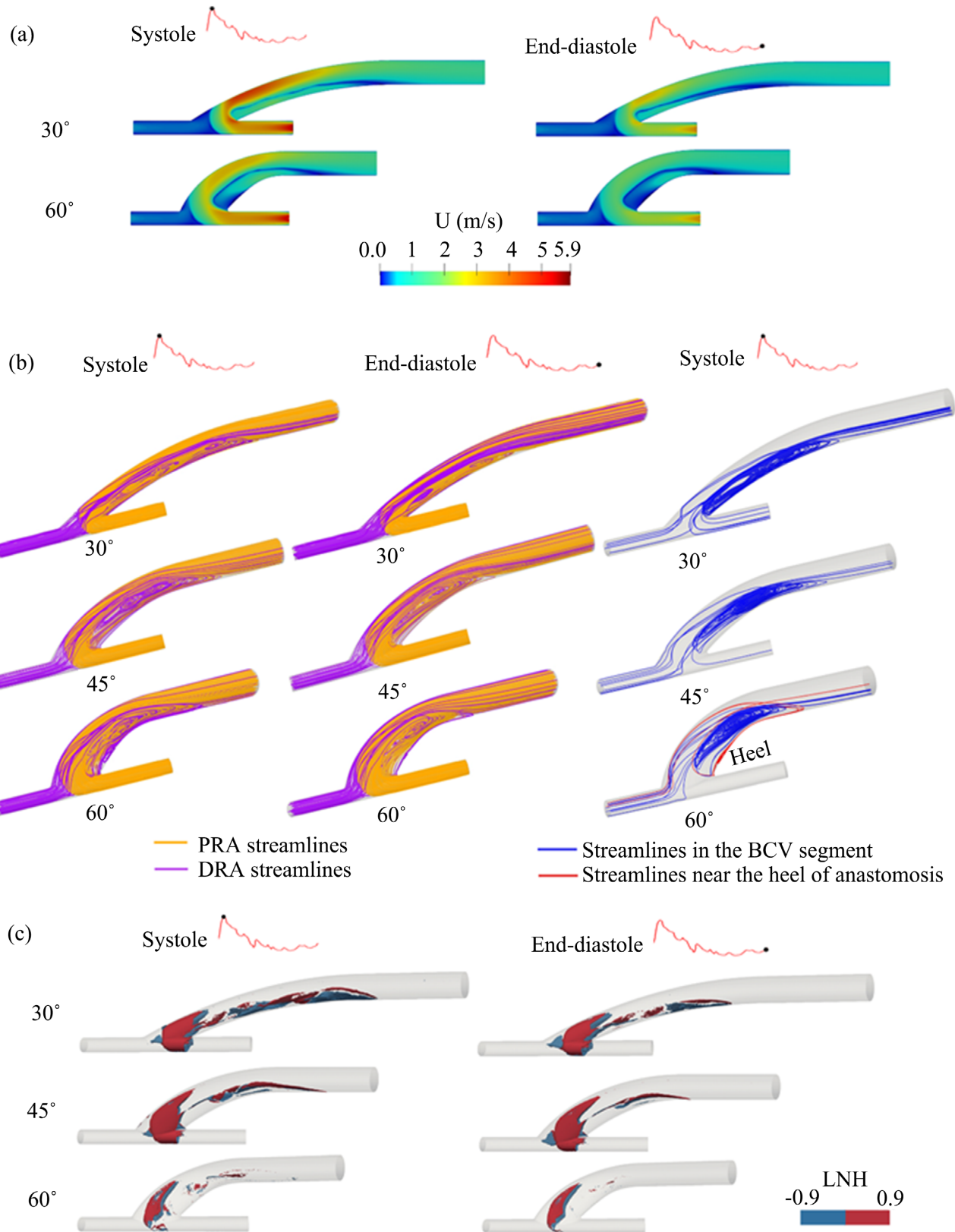


**Figure 4.** Comparisons of hemodynamics in mature models. (a) Velocity fields; (b) Streamlines; (c) LNH distributions.

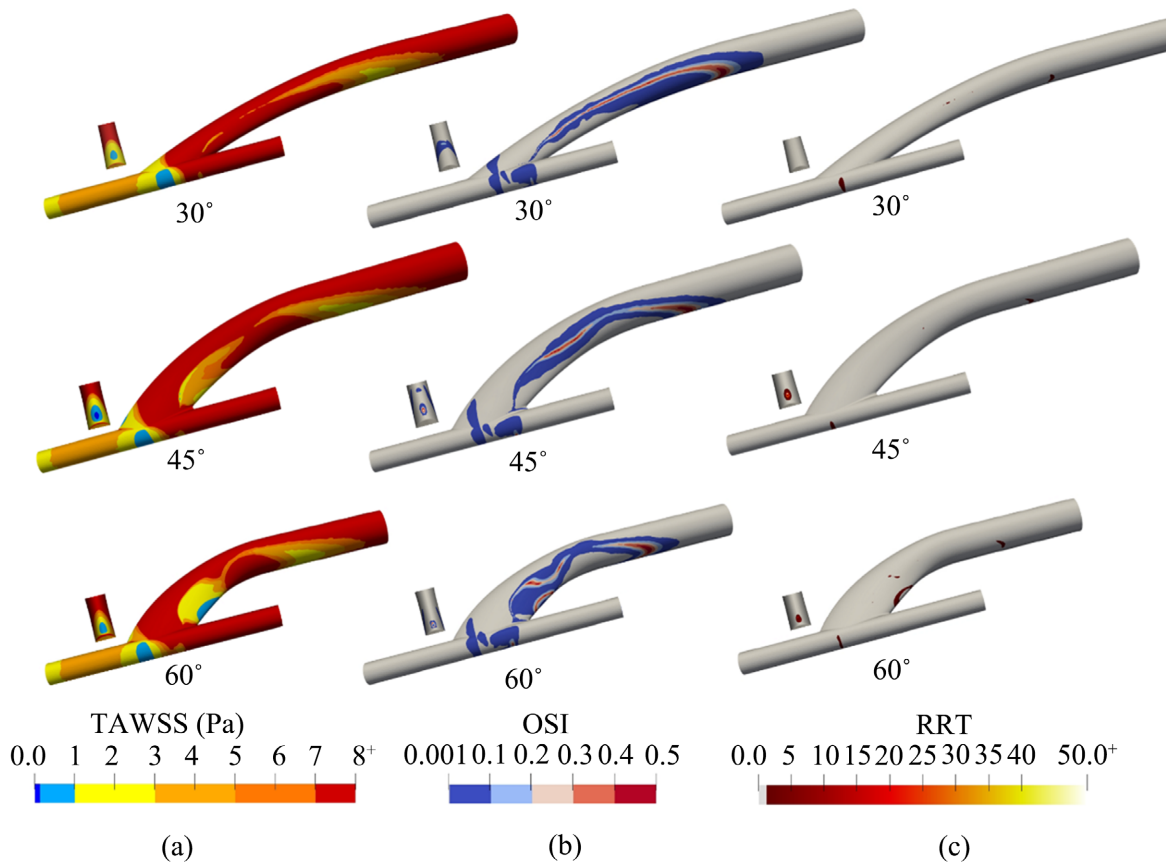


**Figure 5.** Comparisons of WSS biomarkers in mature models. (a) TAWSS distributions; (b) OSI distributions; (c) RRT distributions.

**Table 2.** Comparison of three WSS biomarkers in non-mature models.

$\theta$ (°)	TAWSS						RRT	
	CV			RA			RRT_max <sup>g</sup>	RRT_ave <sup>h</sup>
	Toe_min <sup>a</sup> (Pa)	Heel_min <sup>b</sup> (Pa)	CV_area <sup>c</sup> (mm <sup>2</sup> )	Floor_min <sup>d</sup> (Pa)	Floor_area <sup>e</sup> (mm <sup>2</sup> )	RRT_area <sup>f</sup> (mm <sup>2</sup> )		
30	6.94	-	1.25	2.59	8.56	2.39	9.59	1.74
45	0.5	-	2.78	2.35	8.90	4.23	143.44	2.22
60	1.25	3.17	9.29	2.27	8.02	6.17	79.55	2.57
75	4.80	4.80	7.47	1.75	8.15	5.07	73.46	2.37
90	-	2.80	5.67	1.91	8.31	4.58	54.03	2.34

a. The minimal TAWSS value in low TAWSS region near the toe of anastomose. b. The minimal TAWSS value in low TAWSS region near the heel of anastomose. c. The total area of low TAWSS region in CV. d. The minimal TAWSS value in low TAWSS region near the floor of anastomose. e. The total area of low TAWSS region in RA. f. The total area of RRT larger than 1. g. The maximal RRT value. h. The average RRT value.

Meanwhile, the RRT\_area increases with  $\theta$  until the  $60^\circ$  model and decreases from  $60^\circ$  to  $90^\circ$  models.

The results indicate that the acute angle represents the optimal choice for the mature RCAVF. Despite the differences in hemodynamics and WSS distributions between the non-mature and mature models, the selection of the best  $\theta$  remains unaltered.

### 3.3. Stenosis-Prone Locations (SPL)

As indicated by our results, the SPL in RCAVF can be visualized in **Figure 6**. The sites of early stenoses (pre-stenoses) in non-mature RCAVFs can be categorized into type i and type ii, as depicted in **Figure 6(a)**. The pre-stenosis type i is located in the RA at the floor of the anastomosis and is caused by the convergence of two inlet flows. The sudden change in the boundary at the anastomosis leads to boundary layer separation and the formation of pre-stenosis type ii. Due to the limited increase in blood flow at the PRA inlet and blood vessel diameters during the initial stage, the recirculating region is small and situated near the heel of the anastomosis.

The SPL in mature RCAVFs (post-stenoses) are classified into four types (**Figures 6(b)-(d)**), designated as Types 1 to 4, and their distribution changes with the increase of  $\theta$ . The post-stenosis type 1 appears on the floor of anastomosis and is situated closer to the toe compared to the non-mature model due to the larger energy difference between the two inlets. The lumen area of the BCV segment increases with  $\theta$  augmenting, causing the post-stenosis type 2 produced in the BCV segment near the heel of anastomosis. The post-stenosis type 3 is located at the end of the largest recirculating region in the BCV segment and based on a comparison of three WSS biomarkers, Type 2 stenosis poses a greater risk compared to Type 3 in the case of large- $\theta$  RCAVFs. The post-stenosis type 4 is the most pronounced when  $\theta$  is approximately  $45^\circ$  and decreases as  $\theta$  changes.

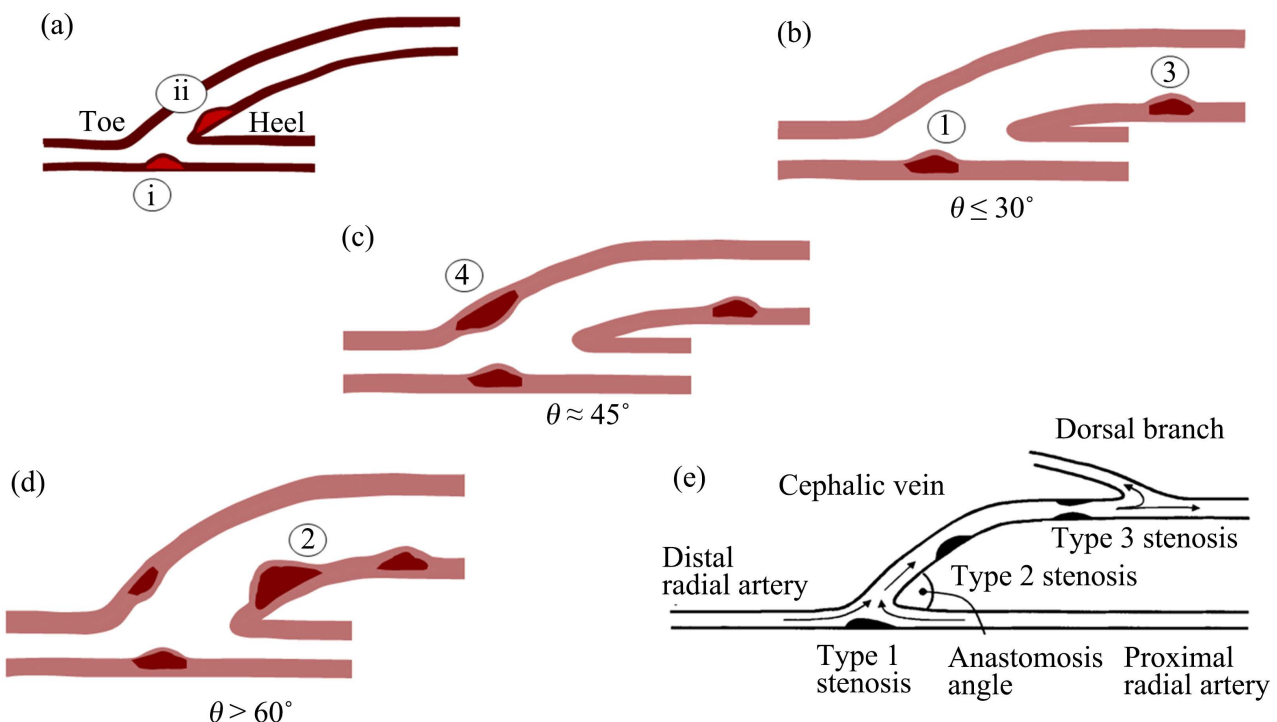


**Figure 6.** The classifications of stenosis-prone locations in RCAVF. (a) The stenosis-prone locations in non-mature RCAVF; (b)-(d) The stenosis-prone locations in mature RCAVF under different anastomotic angles; (e) The specific sites of stenosis in the mature RCAVF identified by a clinical study [8].

We compared our predictions of SPL to a clinical study [8]. The findings of post-stenosis type 1 and type 2 from Sivanesan *et al.* were found to be in agreement with our numerical estimations (Figure 6(e)). The discrepancy in post-stenosis type 3 can be attributed to the absence of consideration of the dorsal branch in our RCAVF models. The post-stenosis type 4, which was predicted in our models, was not reported in the results of the clinical study. This discrepancy may be due to the difficulties of obtaining accurate measurements and defining  $\theta$  in clinical settings. The  $\theta$  in the clinical study was determined as the internal angle of the anastomosis ( $49^\circ$ ), which is smaller than the  $\theta$  definition used in our models. Hence, the results of the clinical study align more closely with those of the  $60^\circ$  RCAVF mature model. In the large- $\theta$  mature models, the risk of post-stenosis type 4 is lower compared to the other post-stenosis types. Additionally, this clinical study [8] only recorded stenoses that resulted in a reduction of the luminal cross-sectional area by more than 40%. This may explain why the stenosis formed at the toe of the anastomosis was not recorded, as it was not obvious.

### 3.4. Clinical Study

A clinical pilot study was conducted with six cases to record the vascular geometric parameters, maturation, and stenosis types (Table 3). The results indicated that three out of six cases matured successfully within six weeks (patients no. 1 to no. 3), while the other three required secondary surgery (patients no. 4 to no. 6). In successful cases, patient no. 1 used a large angle of  $75^\circ$ . Although the fistula successfully matured, two post-stenoses were discovered soon after. The stenosis in the BCV segment near the anastomosis was produced in the same location as post-stenosis type 2, which reduced the lumen diameter to 2.2 mm. The second stenosis was found 16 mm downstream from this stenosis (the same location as post-stenosis type 3). This stenosis reduced the lumen diameter to 2 mm. The surgeon had to perform a surgical correction. Fistulas no. 2 and no. 3 used more acute angles and matured within six weeks. No significant stenosis was found during the follow-up period. A small stenosis was discovered in fistula no. 3 in the same location as post-stenosis type 1 after nine months which did not affect the function of the fistula.

**Table 3.** Comparison of three WSS biomarkers in non-mature models Six RCAVF patient cases provided by Hospices Civils de Lyon.

Patient	Sex	Year of birth	GPs					Maturation in six weeks	Stenosis observation
			$D_{ra}$ (mm)	$D_{cv}$ (mm)	$h$ (mm)	$D_a$ (mm)	$\theta$ ( $^\circ$ )		
No.1	Female	1946	2.5	3.5	45	10	75	Yes	Post-stenoses types 2 and 3 after two months (surgical correction 2 times)
No.2	Male	1987	1.6	3.5	23	10	40	Yes	No stenosis
No.3	Male	1966	1.7	2.5	43	10	10	Yes	Post-stenosis type 1 after nine months
No.4	Male	1955	2.6	2.1	11	10	70	No	Pre-stenoses types i and ii (surgical correction 3 times)
No.5	Female	1942	1.7	3.2	25	10	60	No	Pre-stenosis type ii (surgical correction)
No.6	Male	1973	1.4	2.8	14	10	40	No	Pre-stenoses types i and ii (surgical correction)

In contrast, the fistulas of patients no. 4 and no. 5, created with large angles, exhibited pre-stenosis near the heel of the anastomosis (pre-stenosis type ii). A stenosis at the floor of anastomosis was found simultaneously in patient no. 4 who underwent surgical corrections three times. Similarly, patient no. 6, who used the same angle as patient no. 2, failed to mature due to the presence of two pre-stenoses (the same locations as pre-stenosis types i and ii).

These six cases and the previous clinical research [8] can elementarily validate the SPL predicted by our study. From these six cases, the small- $\theta$  anastomosis is superior to large- $\theta$  anastomosis. However, the final maturation of the fistula relates to not only the anastomotic configuration but also to the patient's vascular status. Patient no. 6 used the same angle as patient no. 2. Because of the significantly larger vessel diameters, the younger age, and better vascular status of patient no. 2, his fistula had a better performance.

#### 4. DISCUSSION

The numerical model predictions suggest that the RCAVF with an acute  $\theta$  may reduce disturbed flow. The LNH analysis demonstrates that blood flow is more stable at the acute  $\theta$ . As  $\theta$  increases, a secondary recirculating region will emerge near the heel of the anastomosis during fistula remodeling. The WSS analysis also indicates that low and oscillating WSSs are minimized in the acute angle model. In the acute  $\theta$ , the limited lumen area of the BCV segment requires most of the DRA inlet blood flow to pass through both sides of the PRA inlet flow, leading to stimulation of the toe by low and oscillating WSSs. As  $\theta$  increases, the hydraulic area of the BCV segment expands, allowing for more DRA inlet fluid to flow parallel with PRA inlet fluid into the BCV segment. This results in reduced negative stimulation near the toe of the anastomosis. However, with the increase in lumen area, the second recirculating region begins to emerge near the heel of the anastomosis.

Previous numerical modeling studies on AVF have primarily focused on simplified and personalized models with postoperative geometries. The simplified models [23, 26] optimized AVF geometric shapes without considering the maturation process and the impact of anastomosis angle ( $\theta$ ) was difficult to determine as the previous research [23] changed both  $\theta$  and the distance between blood vessels ( $h$ ) simultaneously. While personalized models [21, 27] were more representative of reality, the anastomosis configuration was unalterable and modifications to fistula forms could not be made. The present study offers a distinct advantage. Unlike other numerical studies on anastomosis angles, our study is not restricted to a single time point. By analyzing two different maturation time points, we aim to compare the SPL development with varying anastomosis angles during the maturation process, providing surgeons with a more comprehensive understanding of the disturbed fluid within the RCAVF.

The present study has some limitations that must be acknowledged. Our model is idealized, and the results should be applied with caution in the presence of tortuous vessels, complex anatomy, or pre-existing vascular pathologies. The validation of our findings is based on a small cohort of six cases, and a larger sample size would strengthen the generalizability of our results. Further studies are needed to fully explore the implications of our findings in clinical practice. It is important to note that this study is focused on exploring the impact of anastomosis angle on the hemodynamics and WSS distribution during RCAVF maturation and is not a comprehensive clinical study with statistical analysis of patient data.

#### 5. CONCLUSION

Our research has indicated that the use of an RCAVF with an acute angle can enhance the hemodynamic environment and mitigate low and oscillating WSS stimuli during the maturation process. The patterns of SPL and their evolution during the maturation phase, under various values of  $\theta$ , exhibit distinct characteristics. During the initial stage of maturation, early stenosis often manifests near the anastomosis. At the final stage of maturation, the SPL extends to the inlet of the straight vein segment. When  $\theta$  increases to around 45°, the risk of stenosis in the vicinity of the anastomotic toe becomes more pronounced. Further increases in  $\theta$  result in the emergence of another SPL near the anastomotic heel.

## ACKNOWLEDGEMENTS

Thanks to the Chinese government and French National Centre for Scientific Research for funding this research and to the Hospices Civils de Lyon to provide the clinical data for this study and participate in this work.

## CONFLICTS OF INTEREST

The authors declare no conflicts of interest regarding the publication of this paper.

## REFERENCES

1. Atkins, R.C. (2005) The Epidemiology of Chronic Kidney Disease. *Kidney International*, **67**, S14-S18. <https://doi.org/10.1111/j.1523-1755.2005.09403.x>
2. Lok, C.E. and Davidson, I. (2012) Optimal Choice of Dialysis Access for Chronic Kidney Disease Patients: Developing a Life Plan for Dialysis Access. *Seminars in Nephrology*, **32**, 530-537. <https://doi.org/10.1016/j.semephrol.2012.10.003>
3. Schmidli, J., Widmer, M.K., Basile, C., Donato, G., Gallieni, M., Gibbons, C.P., Haage, P., Hamilton, G., Hedin, U., Kamper, L., *et al.* (2018) Editor's Choice—Vascular Access: 2018 Clinical Practice Guidelines of the European Society for Vascular Surgery (ESVS). *European Journal of Vascular and Endovascular Surgery*, **55**, 757-818. <https://doi.org/10.1016/j.ejvs.2018.02.001>
4. Remuzzi, A. and Bozzetto, M. (2017) Biological and Physical Factors Involved in the Maturation of Arteriovenous Fistula for Hemodialysis. *Cardiovascular Engineering and Technology*, **8**, 273-279. <https://doi.org/10.1007/s13239-017-0323-0>
5. Wong, C.-Y., de Vries, M.R., Wang, Y., van der Vorst, J.R., Vahrmeijer, A.L., van Zonneveld, A.J., Roy-Chaudhury, P., Rabelink, T.J., Quax, P.H.A. and Rotmans, J.I. (2014) Vascular Remodeling and Intimal Hyperplasia in a Novel Murine Model of Arteriovenous Fistula Failure. *Journal of Vascular Surgery*, **59**, 192-201.e1. <https://doi.org/10.1016/j.jvs.2013.02.242>
6. Wootton, D.M. and Ku, D.N. (1999) Fluid Mechanics of Vascular Systems, Diseases, and Thrombosis. *Annual Review of Biomedical Engineering*, **1**, 299-329. <https://doi.org/10.1146/annurev.bioeng.1.1.299>
7. Yang, Y., Schiava, N.D., Kulisa, P., Hajem, M.E., Bou-Saïd, B., Simoëns, S. and Lermusiaux, P. (2021) Optimization of Maturation of Radio-Cephalic Arteriovenous Fistula Using a Model Relating Energy Loss Rate and Vascular Geometric Parameters. *Journal of Biomedical Science and Engineering*, **14**, 271-287. <https://doi.org/10.4236/jbise.2021.146023>
8. Sivanesan, S. (1999) Sites of Stenosis in AV Fistulae for Haemodialysis Access. *Nephrology Dialysis Transplantation*, **14**, 118-120. <https://doi.org/10.1093/ndt/14.1.118>
9. Waite, L. and Fine, J.M. (2017) Applied Biofluid Mechanics. 2nd Edition, McGraw Hill Education, New York.
10. Morales, H.G., Larrabide, I., Geers, A.J., Aguilar, M.L. and Frangi, A.F. (2013) Newtonian and Non-Newtonian Blood Flow in Coiled Cerebral Aneurysms. *Journal of Biomechanics*, **46**, 2158-2164. <https://doi.org/10.1016/j.jbiomech.2013.06.034>
11. Kim, S.-W. and Benson, T.J. (1992) Comparison of the SMAC, PISO and Iterative Time-Advancing Schemes for Unsteady Flows. *Computers & Fluids*, **21**, 435-454. [https://doi.org/10.1016/0045-7930\(92\)90048-Z](https://doi.org/10.1016/0045-7930(92)90048-Z)
12. Ochsner, A., Colp, R. and Burch, G.E. (1951) Normal Blood Pressure in the Superficial Venous System of Man at Rest in the Supine Position. *Circulation*, **3**, 674-680. <https://doi.org/10.1161/01.CIR.3.5.674>
13. Wilson, K.E., Tat, J. and Keir, P.J. (2017) Effects of Wrist Posture and Fingertip Force on Median Nerve Blood Flow Velocity. *BioMed Research International*, **2017**, e7156489. <https://doi.org/10.1155/2017/7156489>

14. Beniwal, S., Bhargava, K. and Kausik, S.K. (2014) Size of Distal Radial and Distal Ulnar Arteries in Adults of Southern Rajasthan and Their Implications for Percutaneous Coronary Interventions. *Indian Heart Journal*, **66**, 506-509. <https://doi.org/10.1016/j.ihj.2014.08.010>
15. Willemet, M., Chowienczyk, P. and Alastrauey, J. (2015) A Database of Virtual Healthy Subjects to Assess the Accuracy of Foot-to-Foot Pulse Wave Velocities for Estimation of Aortic Stiffness. *American Journal of Physiology—Heart and Circulatory Physiology*, **309**, H663-H675. <https://doi.org/10.1152/ajpheart.00175.2015>
16. Caro, C.G., Cheshire, N.J. and Watkins, N. (2005) Preliminary Comparative Study of Small Amplitude Helical and Conventional ePTFE Arteriovenous Shunts in Pigs. *Journal of the Royal Society Interface*, **2**, 261-266. <https://doi.org/10.1098/rsif.2005.0044>
17. Gallo, D., Steinman, D.A., Bijari, P.B. and Morbiducci, U. (2012) Helical Flow in Carotid Bifurcation as Surrogate Marker of Exposure to Disturbed Shear. *Journal of Biomechanics*, **45**, 2398-2404. <https://doi.org/10.1016/j.jbiomech.2012.07.007>
18. Cunnane, C.V., Cunnane, E.M., Moran, D.T. and Walsh, M.T. (2019) The Presence of Helical Flow Can Suppress Areas of Disturbed Shear in Parameterised Models of an Arteriovenous Fistula. *International Journal for Numerical Methods in Biomedical Engineering*, **35**, e3259. <https://doi.org/10.1002/cnm.3259>
19. De Nisco, G., Kok, A.M., Chiastra, C., Gallo, D., Hoogendoorn, A., Migliavacca, F., Wentzel, J.J. and Morbiducci, U. (2019) The Atheroprotective Nature of Helical Flow in Coronary Arteries. *Annals of Biomedical Engineering*, **47**, 425-438. <https://doi.org/10.1007/s10439-018-02169-x>
20. Bozzetto, M., Ene-Iordache, B. and Remuzzi, A. (2016) Transitional Flow in the Venous Side of Patient-Specific Arteriovenous Fistulae for Hemodialysis. *Annals of Biomedical Engineering*, **44**, 2388-2401. <https://doi.org/10.1007/s10439-015-1525-y>
21. Ene-Iordache, B., Semperboni, C., Dubini, G. and Remuzzi, A. (2015) Disturbed Flow in a Patient-Specific Arteriovenous Fistula for Hemodialysis: Multidirectional and Reciprocating Near-Wall Flow Patterns. *Journal of Biomechanics*, **48**, 2195-2200. <https://doi.org/10.1016/j.jbiomech.2015.04.013>
22. Lee, S.-W., Antiga, L. and Steinman, D.A. (2009) Correlations among Indicators of Disturbed Flow at the Normal Carotid Bifurcation. *Journal of Biomechanical Engineering*, **131**, Article ID: 061013. <https://doi.org/10.1115/1.3127252>
23. Ene-Iordache, B., Cattaneo, L., Dubini, G. and Remuzzi, A. (2013) Effect of Anastomosis Angle on the Localization of Disturbed Flow in “Side-to-End” Fistulae for Haemodialysis Access. *Nephrology Dialysis Transplantation*, **28**, 997-1005. <https://doi.org/10.1093/ndt/gfs298>
24. Chiu, J.-J. and Chien, S. (2011) Effects of Disturbed Flow on Vascular Endothelium: Pathophysiological Basis and Clinical Perspectives. *Physiological Reviews*, **91**, 327-387. <https://doi.org/10.1152/physrev.00047.2009>
25. Ene-Iordache, B. and Remuzzi, A. (2012) Disturbed Flow in Radial-Cephalic Arteriovenous Fistulae for Hemodialysis: Low and Oscillating Shear Stress Locates the Sites of Stenosis. *Nephrology Dialysis Transplantation*, **27**, 358-368. <https://doi.org/10.1093/ndt/gfr342>
26. Carroll, J., Varcoe, R.L., Barber, T. and Simmons, A. (2019) Reduction in Anastomotic Flow Disturbance within a Modified End-to-Side Arteriovenous Fistula Configuration: Results of a Computational Flow Dynamic Model. *Nephrology*, **24**, 245-251. <https://doi.org/10.1111/nep.13219>
27. Rathore, S., Uda, T., Huynh, V.Q.H., Suito, H., Watanabe, T., Sugiyama, H. and Srikanth, D. (2021) Numerical Computation of Blood Flow for a Patient-Specific Hemodialysis Shunt Model. *Japan Journal of Industrial and Applied Mathematics*, **38**, 903-919. <https://doi.org/10.1007/s13160-021-00469-9>